Multiple Coulomb phase in the fluoride pyrochlore CsNiCrF6

Multiple Coulomb phase in the fluoride pyrochlore $CsNiCrF_6$

T. Fennell[1*], M. J. Harris[2], S. Calder[3], M. Ruminy[1], M. Boehm[4], P. Steffens[4], M.-H. Lemée-Cailleau[4], O. Zaharko[1], A. Cervellino[5], S. T. Bramwell[6]

[1]Laboratory for Neutron Scattering and Imaging, Paul Scherrer Institut, 5232 Villigen PSI, Switzerland

[2]School of Divinity, University of Edinburgh, New College, Mound Place, Edinburgh, EH1 2LX, UK

[3]Quantum Condensed Matter Division, Oak Ridge National Laboratory, Oak Ridge, Tennessee 37831, USA

[4]Institut Laue-Langevin, 71 avenue des Martyrs, CS 20156, 38042 Grenoble cedex 9, France

[5]Swiss Light Source, Paul Scherrer Institut, 5232 Villigen PSI, Switzerland

[6]London Centre for Nanotechnology and Department of Physics and Astronomy, University College London, 17-19 Gordon Street, London WC1H 0AH, UK

* tom.fennell@psi.ch

The Coulomb phase is an idealized state of matter, whose properties are determined by factors beyond conventional considerations of symmetry, including global topology, conservation laws and emergent order. Theoretically, Coulomb phases occur in ice-type systems like ice and spin ice; in dimer models; and certain spin liquids. However, apart from ice-type systems, more general experimental examples are very scarce. Here we study the partly-disordered material $CsNiCrF_6$ and show that this material is a multiple Coulomb phase with signature correlations in three degrees of freedom: charge configurations, atom displacements, and spin configurations. We use neutron and x-ray scattering to separate these correlations, and to determine the magnetic excitation spectrum. Our results show how the structural and magnetic properties of apparently disordered materials may inherit, and be dictated by, a hidden symmetry – the local gauge symmetry of an underlying Coulomb phase.

The correlations and dynamics of conventional phases of matter can be summarized in terms of broken symmetries [1] and the transverse (Goldstone) and longitudinal (Higgs) fluctuations of their associated order parameters [2]. By contrast, in a Coulomb phase [3], there is no long-range order and the cooperative behavior of the local degrees of freedom is best described by a field, whose emergent symmetry is that of the electromagnetic field. Any ground state of the local degrees of freedom can be represented by a non-divergent field (i.e. div$\mathbf{B}$=0, see Fig. 1A), which means that although the Coulomb phase has no broken global symmetry, it has local gauge symmetry and the closed loop topology of the associated field lines [3,4,5]. Dynamics involve coherent fluctuations of the field, or topological defects in the field, which can respectively be identified as generalized photons and charges of the relevant field theories [6,7,8].

Although the charge ice [9,10] (Fig. 1B) and the pyrochlore Heisenberg antiferromagnet [11] (Fig. 1C) are two of the best-known predicted Coulomb phases, neither has a good experimental model system. Theoretical investigations of the pyrochlore Heisenberg antiferromagnet highlight the generalities of Coulomb phases [11,12,13,14,15]. The spin correlation function has the power-law behavior generic to all Coulomb phases, implying that there should be `pinch-points' in the static structure factor [3,12,16,17]. Creation of topological defects in the flux fields (monopoles, though in this case not discretized as they are in spin ice [18,19,20]) modifies the magnetic charge density locally, and relaxation of this disturbance leads to a monopole current. The associated spin relaxation rate depends only on temperature (i.e. it exhibits E/T scaling) and occurs at many wave vectors, including the pinch points, as shown by the theoretical spin relaxation function $S(\mathbf{Q},t)/S(\mathbf{Q},0)$ [14,15] illustrated in Fig. 2A. On nodal lines connecting the pinch points, different behaviors are found. In a cut through the simulated $S(\mathbf{Q},\omega)$ along a nodal line, as shown in Fig. 2B [15], the relaxational response at the zone centre gives way to spin diffusion at small wave vectors where fluctuations conserve the local magnetization; fast, quasi-dispersive dynamics due to remnant spin waves appear further along the nodal lines. It was recently suggested that the lattice dynamics of solids with correlated disorder (including charge ices) may be of interest for functional properties such as thermoelectricity [21], but the vibrational analogs of general Coulomb phase dynamics have not been investigated. Moreover, in dense spin systems with mixed cations such as Y_2CrSbO_7 or $YbMgGaO_4$, site and bond disorder clearly have important consequences for the magnetic properties [22,23,24]. These materials are suggested to have random disorder, but although correlated disorder may be difficult to detect, it is highly probable because the long-range nature of the Coulomb interaction makes it divergent in the presence of random disorder. Further investigations of such materials may well emphasize the importance of understanding spin systems that live on structures with correlated disorder.

In this work, we use x-ray and neutron scattering to investigate correlations and dynamics in $CsNiCrF_6$, in which Ni^{2+} and Cr^{3+} jointly occupy a pyrochlore lattice. $CsNiCrF_6$ was suggested to be a pyrochlore Heisenberg antiferromagnet [25,26] before the concept of a Coulomb phase emerged. However, even in the simplest description [27], Ni-Ni, Ni-Cr and Cr-Cr superexchange constants form a set of different values, breaking the local degeneracy of the true pyrochlore Heisenberg antiferromagnet that is crucial to the formation of a Coulomb phase. However, with two ions of different charge on the pyrochlore lattice, $CsNiCrF_6$ is a candidate charge ice and later we show how a magnetic Coulomb phase is inherited from the charge ice structural correlations.

The charge ice structure can be addressed in two ways: the average crystal structure can be studied by conventional diffraction experiments, and departures from the average due to

(correlated) disorder can be investigated by measuring structural diffuse scattering [28]. To investigate the average structure, we performed single crystal neutron diffraction and synchrotron powder x-ray diffraction experiments. Refinement of crystallographic models against these data indicate three features: firstly, the average structure is well described by that of the mixed metal fluoride pyrochlores (see Fig. 1D,E), with isotropic displacement parameters [29]; secondly, the thermal displacement factor of the Cs^{+} ion is by far the largest of all the atoms, and is strongly thermally activated; lastly, split site models in which ions partially occupy a lower symmetry site around the expected position, as in other pyrochlore materials with structural disorder [30] are not stable or do not improve the refinement. Further details of the refinements are given in the supplementary information [31].

If there is sufficient contrast in neutron scattering length between the two cations, as is the case for Ni (b_c=10.3 barn) and Cr (b_c=3.6 barn), there should be a direct signature of charge ice correlations in the structural (i.e. nuclear) diffuse neutron scattering. We used polarized neutron scattering to separate structural and magnetic scattering. The structural diffuse scattering is shown in Fig. 3A, and its form indicates that non-trivial structural correlations are present. In the experimental data the intensity of the diffuse features generally increases with the magnitude of the wavevector, while a model calculation of a charge ice with only substitutional correlations (Fig. 3B) has diffuse features with similar weight across the whole pattern. The calculation has pinch points at (-2,-2,0) and (0,0,2), whose existence and position are the defining features of a structural Coulomb phase on the pyrochlore lattice [3]. We can identify one of these pinch points in the experimental data. In Fig. 3A, a triangular region of intensity around (h,h,0) sharpens inward, towards (2,2,0). Cuts through the experimental data (Fig. 3D) confirm that the scattering sharpens toward the (2,2,0) Bragg point, and that this feature is therefore a type of pinch point. The very weak intensity of the inner part of the pattern prevents us from concluding on the exact nature of the features around (0,0,2), but the intense diffuse scattering pinching in toward (0,0,6) at the limit of our wave vector coverage suggests another pinch point, as expected from the calculation. The pinch points are the essential characteristic of the Coulomb phase, indicating the long-range coherence of the ice rules, their presence in the experimental data shows unambiguously that a structural Coulomb phase is present.

The other, more diffuse, features characterize short-wavelength correlations or local structures that exist within the Coulomb phase, and the distribution of intensity in the experimental pattern compared to the calculation shows that the structure contains contributions beyond purely ice-rule obeying cation configurations. When working with single crystal diffuse scattering data with relatively limited wave vector access, numerical modelling in direct space is most convenient [32, 33, 34, 35], and we propose a simple model that explains our structural observations reasonably well. From the point of view of the bond valence sum [36], the average structure is an efficient compromise: no cation has a fully favorable bond valence sum, but all are close to their optimal values. If ice rule cation correlations exist amongst Ni^{2+} and Cr^{3+}, we can make a local distortion throughout the structure (Fig. 1D) that brings the bond valence sum of both cations to their optimal values. The Ni/Cr cations have octahedral coordination, sharing four F^{-} with cations of the other type and two with cations of the same type. We assume only that any F^{-} shared between a Ni^{2+}-Cr^{3+} pair is displaced (always by the same amount) toward the Cr^{3+}, sufficient to simultaneously optimize the bond valence sum of all Ni^{2+} and Cr^{3+} ions. The displacement is small enough to lie within the radius of the isotropic displacement parameter, consistent with the absence of a split site in structural refinements or Fourier difference maps. Then, if we search for the locus of sites optimizing the bond valence sum for each Cs^{+}, we find it takes the form of one or more connected loops on the surface of a

sphere, with the average over all Cs^+ sites making a hollow spherical shell. As in other such cases, the radius of the shell is larger than the displacement parameter of the atom in the average structure [37].

The introduction of the cation correlations and local distortion of the octahedra has a strong effect on the calculated structural diffuse scattering - the local distortions redistribute the weight of the pure configurational disorder pattern towards larger wave vector, suppressing the part in the center of the pattern (Fig. 3C) but leaving the pinch point at (2,2,0) described above. Furthermore, the combination of cation correlations and local anion displacements modifies the topology of the available Cs^+ positions from discrete pockets in the average structure (i.e. a split site), to continuous displacements on the surface of a sphere, which on average resembles a large, isotropic displacement parameter as observed. If the framework cations are random, the local distortions still improve the bond valence sums, and still have the same effect on the Cs^+ displacement topology, but the diffuse scattering is a featureless response from the random cations convoluted with weighting to larger wave vector due to the displacements.

Every tetrahedron has four edges with a displacement and two without, a condition that can readily be represented by an ice rule on a single tetrahedron, but the relationship between ice rule and fluxes requires a sign change in `up' and `down' tetrahedra, since anions are displaced toward a cation in both of the tetrahedra of which the cation is a member. An alternative identification of the Coulomb phase in the displacements can be made: the edges of the tetrahedra with a non-displaced F^- anion (or matching cations at each end) select two of the links of the diamond lattice that terminate at the diamond lattice point at the center of the tetrahedron (Fig. 1D); each cation is a member of another such pair on adjacent tetrahedra, similarly selecting two diamond lattice links on these tetrahedra (Fig. 1D, E); tracing the network of diamond lattice links selected in this way reveals a fully packed loop model. Every link of the diamond lattice is a member of a loop and each diamond lattice point is visited by precisely two loops; a given loop is populated only by one type of cation. The same fully packed loop model is obtained by coloring, in two colors, the links of the diamond lattice that host in or out spins in a spin ice [38]. Fully packed loop models represent an intriguing type of correlated disorder, which has so far found experimental relevance only in two dimensions [39,40]. In $CsNiCrF_6$, this displacement ice must play an important role in the exchange interactions and their disorder. The ideal pyrochlore Heisenberg antiferromagnet has a single exchange parameter, but here we can expect three, one each for Ni-Ni, Ni-Cr and Cr-Cr bonds. The required theory will not be one of random disorder of exchange strengths, but of a strongly correlated spatial distribution of exchanges, whose structure is encoded by the fully packed loop model [27].

Our model does not reproduce every aspect of the structural diffuse scattering pattern, but the form of the experimental data and improvements made over the simple charge ice calculation suggest the basic ingredients – a charge ice of Ni^{2+} and Cr^{3+}, displacements of the F^- anions that inherit Coulomb phase correlations from the underlying charge ice, and Cs^+ ions disordered over the surface of a spherical shell around the cage centers – are correct. However, the model is very simple: the ice rules are assumed to operate perfectly (some additional consideration of this point can be found in the supplementary information [31]), with complete degeneracy amongst all microstates (which is known not to be the case in spin ice); the same F^- displacement is made throughout the structure, irrespective of the symmetry of the local distortion - $O_h \rightarrow D_{4h}$ and $O_h \rightarrow C_{2v}$ may both occur depending on the configuration of displaceable F^- ions around each Cr^{3+} and may in reality be differently favorable; and the Cs^+ ions are completely decoupled from the framework.

From the point of view of magnetism, the Curie-Weiss temperature (-70 K) suggests that in $CsNiCrF_6$, the magnetic moments of two sizes (Ni^{2+} has S=1, Cr^{3+} has S=3/2) distributed according to the ice rules, interact antiferromagnetically on average. Separation of the magnetic diffuse scattering by polarized neutron scattering shows that the spins also form a Coulomb phase. The static magnetic correlations exposed in a measurement of $S(\mathbf{Q})$ contain pinch points, and a distribution of intensity similar to the pyrochlore Heisenberg antiferromagnet, as shown in Fig. 4A and B. The existence of pyrochlore Heisenberg antiferromagnet-like correlations in a system with two different interacting ions (distributed according to the ice rules/fully packed loop model) has been justified by numerical simulations for an extensive range of interaction parameters (see regime IV in Ref. [27]). It is clear from our results that $CsNiCrF_6$ falls within this range. As discussed in Ref. [27], the Coulomb phase correlations of the spin system are here inherited from the underlying structural Coulomb phase and do not reflect the degeneracy of the Heisenberg manifold.

This conclusion is supported by a study of the magnetic dynamics using inelastic neutron scattering. Previous studies have shown that there is considerable spectral weight at an energy transfer of ~0.5 meV [26], and in Fig. 5A we show a map of the intensity at constant energy transfer of 0.5 meV. This measurement shows that the spin fluctuations have a structure factor very similar to the static correlations of the Coulomb phase, implying degenerate fluctuations of both long and short wavelength. Constant wave vector scans were used to further investigate the form of $S(\mathbf{Q},\omega)$. The locations of these scans are summarized in Fig. 2A, they probe the nodal lines (h,h,-h) and (0,0,l), including pinch points at (1,1,-1) and (0,0,-2), and generic points on the intense structure factor of Fig. 5A. In Fig. 5B, we show scans measured at the pinch points and generic points. We have converted $S(\mathbf{Q},\omega)$ to $\chi''(\mathbf{Q},\omega)$ in order to simplify model-free interpretations. The data from all these points can be fitted by gapless quasi-elastic Lorentzians with the same width, indicating that the relaxation rate is independent of wave vector (but the intensity varies with position, as expected from Fig. 5A). In Fig. 5C we show a series of scans along a nodal line from a pinch point at (1,1,-1) toward the adjoining regions with no scattering in Fig. 5A (i.e. (0,0,0) or (2,2,-2)). Here we see that the gapless behavior at the pinch point is preserved at small wave vector relative to the pinch point (e.g. (1.1,1.1,-1.1), but a broad peak with a distinct dispersion appears beyond this. Beyond (1.5,1.5,-1.5), the peak becomes very weak and much broader, dispersing back downward as far as it can be followed. The temperature dependence of the width of the susceptibility at two generic wavevectors is linear with the temperature, as shown in Fig. 5D, with a finite response at the lowest temperature. The width of the dispersive feature has essentially the same temperature dependence. In Fig. 5E we summarize our data for nodal lines, showing the sinusoidal dispersion of the fast dynamics.

$CsNiCrF_6$ affords the possibility of studying the dynamics of a magnetic Coulomb phase with full wave vector and frequency information. Interestingly, many features of these dynamics are similar to those of the classical spin liquid phase of the pyrochlore Heisenberg antiferromagnet. In particular, monopole current density is signified by the wave vector-independent relaxation rate with linear temperature at generic wave vectors [14]. Along the nodal lines, the response at and close to the pinch point is gapless. This is consistent with the presence of relaxational dynamics at the pinch point and diffusional dynamics at small wave vector but more extensive measurements would be required to confirm the expected data collapse for spin diffusion. We clearly see a feature that disperses up from the pinch point. The dispersion on the nodal lines is periodic with respect to the pinch points (and identical for the two nodal lines). When compared qualitatively with the prediction of Fig. 2B [14, 15], the

observation of a quasi-linear or sinusoidal dispersion up to the maximum, followed by a collapse into a very broad, weak and downward dispersing intensity is as expected. This dispersive feature represents a fast contribution to the dynamics that can be thought of as a spin wave fluctuation about the local ground state. It is broad in both wave vector and energy since the ground state is not ordered [14].

It may seem remarkable that the delicate-sounding predictions of the pyrochlore Heisenberg antiferromagnet are robust to the strongly correlated structural disorder that we have also described. However, the fully packed ion loops of a charge ice still give rise to a magnetic Coulomb phase of antiferromagnetic character [27], and conserved or topological quantities are closely related to those of the Heisenberg model, leading to similar emergent physics. The expected clear departure from the classical pyrochlore Heisenberg antiferromagnet behavior is, however, manifest in the temperature dependence of the relaxation rate at the generic wavevectors. This quantity is predicted to be simply proportional to the temperature and vanish as $T \rightarrow 0$ [14,15], but we find a weaker temperature dependence and residual response at the lowest temperature.

Below T=2.3 K magnetization measurements on $CsNiCrF_6$ exhibit a history dependence that is reminiscent of canonical spin glasses [25]. A slowing component of dynamics that coexists with the processes we measure here, and which falls into the time window of a magnetization experiment at this temperature seems by no means inconsistent with Ref. [25], but the significant inelastic spectral weight that we observe both above and far below this temperature precludes that $CsNiCrF_6$ is a canonical spin glass [25,26]. Given the relatively small spin sizes, the lowest temperature response may indicate that a quantum spin liquid [41] replaces the classical one.

We have shown that $CsNiCrF_6$ supports multiple Coulomb phases – a charge ice and associated displacement ice, and a magnetic Coulomb phase with antiferromagnetic character. Despite being composed of fully-packed loops of distinct spins, the magnetic Coulomb phase shows dynamical signatures of the pyrochlore Heisenberg antiferromagnet, a classical spin liquid of much higher local symmetry. Our results show how two systems that look completely different from a structural chemistry perspective, may nevertheless share many of the same physical properties, the key connection being the robust local gauge symmetry of the Coulomb phase and its associated conservation laws.

Predictions of wave vector-dependent dynamics of a classical antiferromagnetic Coulomb phase have not previously been examined experimentally (although we note very recent work on a possible quantum analogue, $NaCaNi_2F_7$ [42]). The consequences of ice-rules disorder in the vibrational dynamics (of the framework) have not been examined experimentally or theoretically, but the interplay of framework and caged-atom dynamics are well known to contribute to advantageous thermoelectric properties in skutterudite and clathrate compounds such as $CeFe_4Sb_{12}$ [43], and superconductivity in the analogously structured osmate pyrochlores such as KOs_2O_6 [44]. The chemical flexibility of the fluoride pyrochlore crystal structure (which includes the possibilities of significantly varying the magnetic properties with numerous combinations of transition metal cations, replacing the alkali metal cation with a guest of quite different character such as NH_4^+, or extracting it, as in FeF_3, and of exploring charge ordered versions using compositions such as AFe_2F_6 [45,46], perhaps with a view to metallization) suggests that these compounds are of considerable interest for exploration of both unconventional spin dynamics, and new functionalities based on correlated disorder.

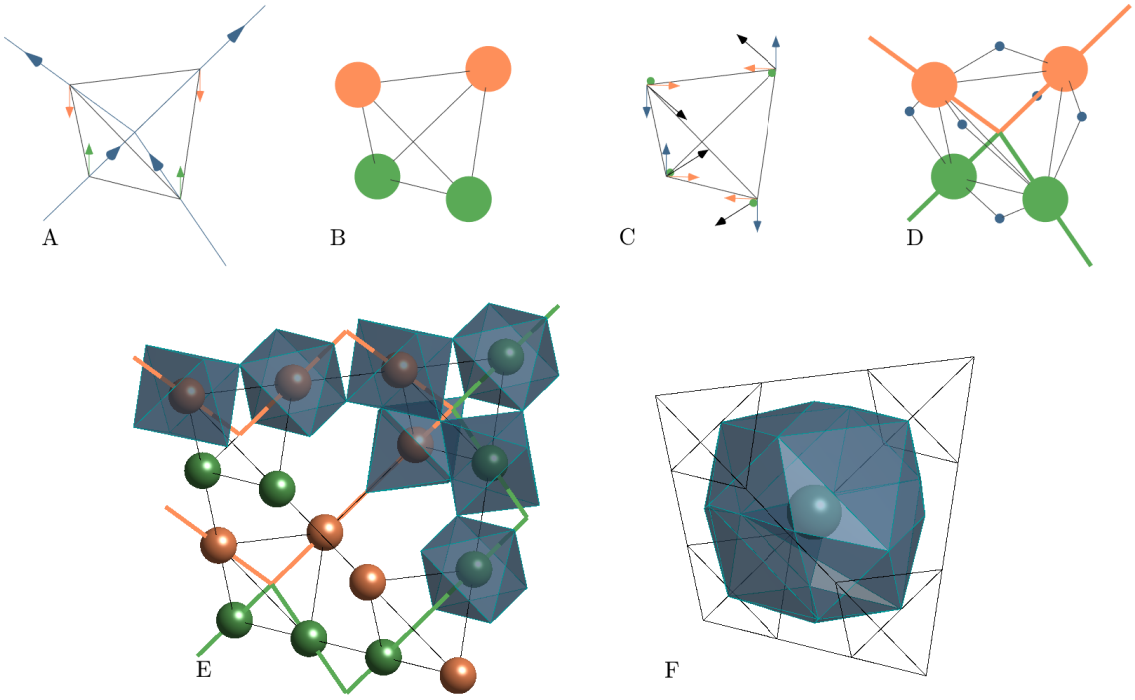

Fig. 1. Illustration of Coulomb phase construction/mappings and structural features of $CsNiCrF_6$. A: The pyrochlore lattice (medial) consists of corner-sharing tetrahedra, on which a Coulomb phase is established when the local degrees of freedom can be represented by a non-divergent field derived from lattice fluxes on the diamond lattice (parent) [3]. A non-divergent configuration of flux variables (blue arrows) around a diamond lattice point is equivalent to the ice rule for spins in a spin ice (two-in-two-out). Antiferromagnetic pseudo-spins are related to the flux variables and configured two-up-two-down in a Coulomb phase ground state (green and orange arrows). B: Two cations occupying the pyrochlore lattice form a charge ice, with cation configurations directly related to the pseudo-spins (green and orange spheres). C: Vector spins coupled antiferromagnetically on the pyrochlore lattice (i.e. a pyrochlore Heisenberg antiferromagnet) must satisfy the condition that the total magnetization of every tetrahedron is zero (black arrows), which can be ensured if the $S_{x,y,z}$ vector components are each represented by a family of pseudospins that obey the ice rule (blue, green and orange arrows). D: In the structure of $CsNiCrF_6$, F^- anions (small blue spheres) are coordinated to two cations (orange spheres are Cr^{3+}, green spheres are Ni^{2+}). The bond valence sum requirements of the cations can be satisfied by displacing anions shared by a pair of unlike cations towards the cation with larger charge (Cr^{3+}). Anions shared between a pair of like cations are not displaced. The edges with non-displaced anions form a fully packed loop model (described in text) on the diamond lattice (green and orange lines). E: The structure of $CsNiCrF_6$ is composed of the pyrochlore lattice of cations, coordinated by octahedra of F^- ions. The octahedra share each of their vertices with another octahedron, forming tetrahedra of tilted octahedra. (Extended sections of the fully packed loop model are shown and the octahedra are drawn undistorted.) F: The structure contains large cages in which the Cs^+ ions reside. The cage coordination is by 18 F^- ions, forming an octahedron that is truncated and capped with rectangular pyramids.

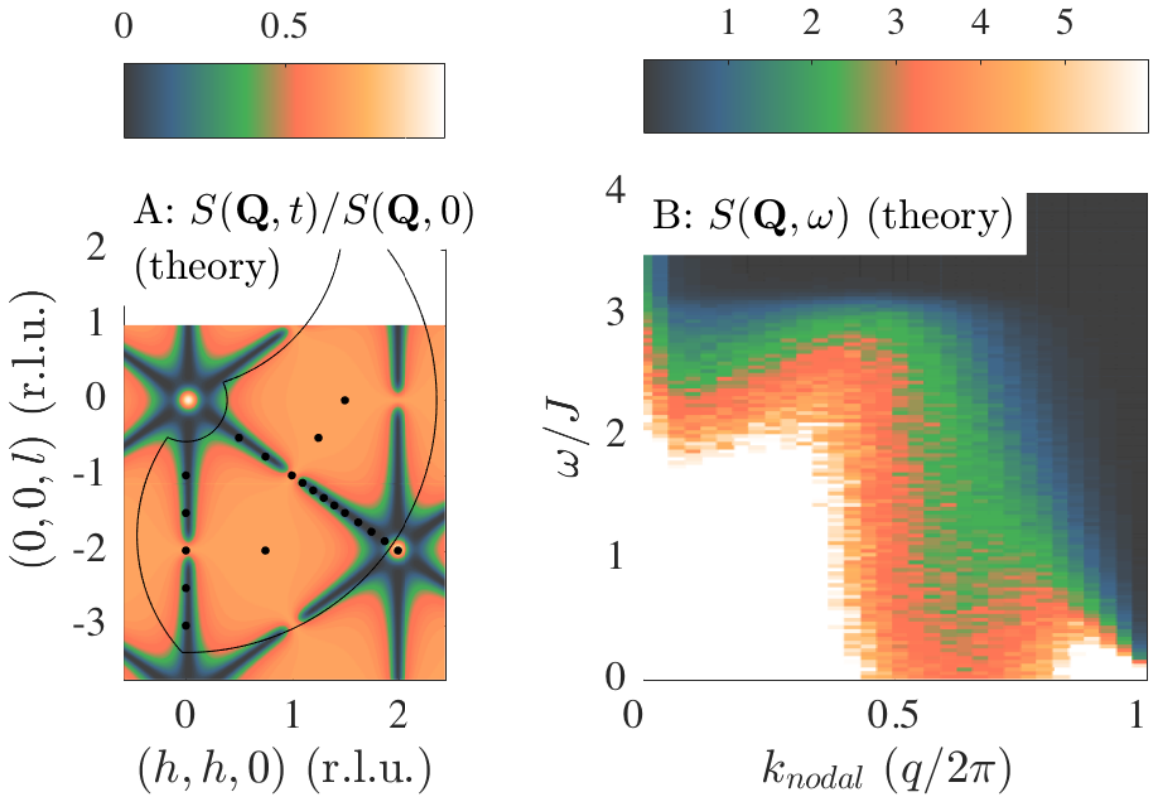

Fig. 2. Illustration of theoretical predictions of the dynamical response of the pyrochlore Heisenberg antiferromagnet. The relaxation function $S(\mathbf{Q},t)/S(\mathbf{Q},0)$ (from [15]) has large regions of reciprocal space where identical relaxation times are expected. The normalization highlights that the scattering function at these wavevectors will have the same width, even if their structure factor is different. The nodal lines, where different dynamical regimes are found, can be clearly seen. The extent (curved lines) and positions (dots) of our mapping and scanning measurements are also shown. B: A sketch of the spectrum along a nodal line (i.e. $(h,h,-h)$) (from [15]) shows the crossovers from gapless relaxational dynamics at the pinch point ($\mathbf{k}_{nodal}=0$), to gapless diffusional dynamics at small $|\mathbf{k}|$, to quasi-dispersive fast dynamics toward $|\mathbf{k}|=0.5$, with broad and weak signal for $|\mathbf{k}|>0.5$.

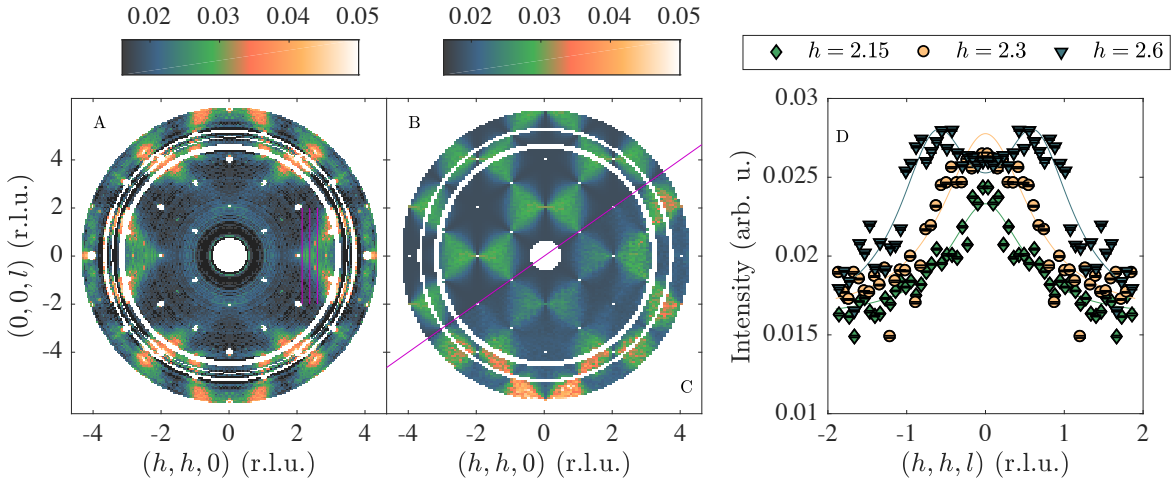

342

343 **Fig. 3**. Structural diffuse scattering in $CsNiCrF_6$. A: The structural diffuse neutron scattering
344 measured at 1.5 K (note that the colour scale starts at 0.01 (arbitrary units) to highlight the
345 weak diffuse scattering around (1,1,1) and (0,0,2), there is a significant wavevector
346 independent diffuse contribution which may arise from isotope incoherent scattering,
347 uncorrelated Cs^+ ions, and/or ice rule defects). B: Predicted diffuse scattering of a charge ice
348 with substitutional correlations only. C: Diffuse scattering calculated for a model with charge
349 ice cation correlations and associated bond valence sum-restoring F^- and Cs^+ displacements. In
350 B and C the calculated intensity is multiplied by a scale factor and a wavevector independent
351 contribution added. D: Cuts through the experimental data (positions indicated by lines on A)
352 show that the feature around (*h*,*h*,0) sharpens inward toward the (2,2,0) position, and is,
353 therefore, the pinch point visible at that position in B and C. Error bars in D are obtained by
354 standard propagation of the Poisson counting statistics of all the measurements (sample,
355 background, calibrants) required to extract the structural scattering cross section.

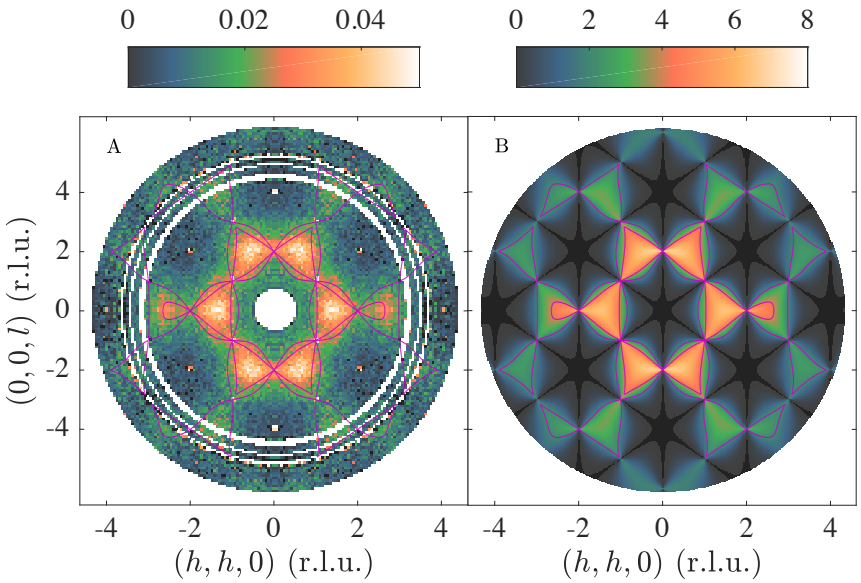

356

357 **Fig. 4.** Magnetic diffuse scattering in $CsNiCrF_6$. A: The experimental magnetic diffuse neutron
358 scattering measured at 1.5 K. B: Model calculation of the structure factor of the pyrochlore
359 Heisenberg antiferromagnet (including the average magnetic form factor for Ni^{2+} and Cr^{3+})
360 [16]. The calculation is for T=0 and incorporates no structural disorder or modulation of the
361 magnetic moment size by site, so its pinch points are extremely sharp and better defined than

those in the experimental data. Isointensity contours from the calculation are superimposed on the experimental data as guides to the eye.

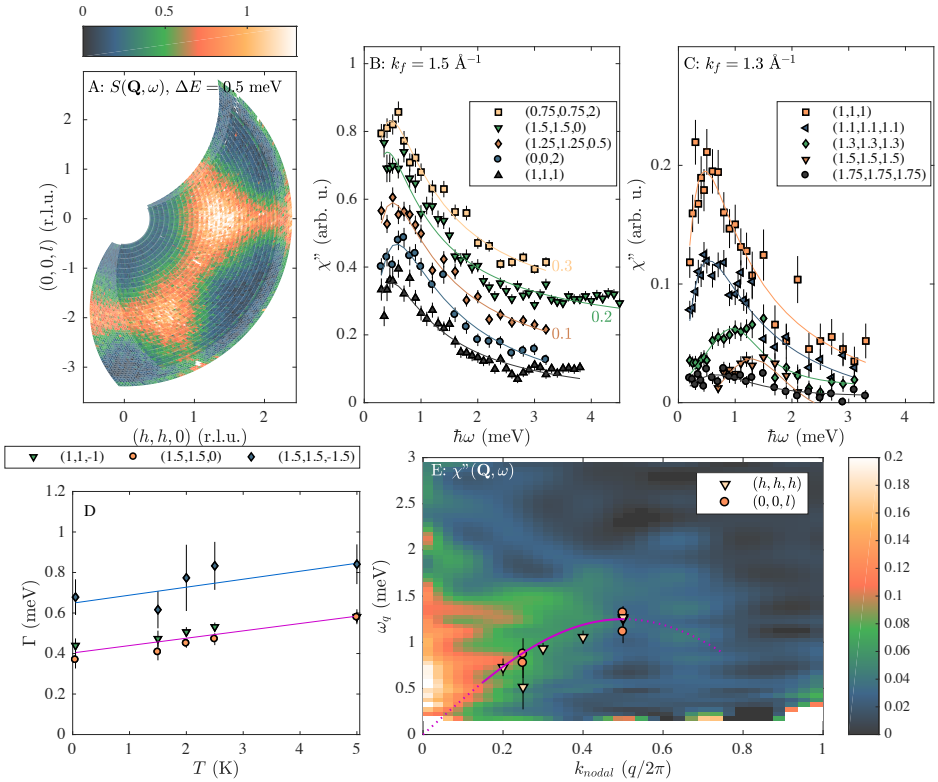

Fig. 5. Wave vector and temperature dependence of magnetic dynamics in $CsNiCrF_6$. A: A map of $S(\mathbf{Q},\omega)$ at a constant energy transfer of 0.5 meV shows a structure factor very similar to the static correlations shown in Fig. 4, but with broadened pinch points. B: Constant wave vector scans at pinch points and points on the structure factor of panel A where relaxational dynamics are expected (see Fig. 2) all have the same width (small numbers adjacent to a data series indicate an arbitrary offset that has been applied to help distinguish them, the real intensity of these series is essentially identical, lines are fits to a gapless quasielastic Lorentzian line shape). C: Constant wave vector scans along the nodal line $(h,h,-h)$ show a gapless spectrum at small $|\mathbf{kl}|$, followed by an upward dispersive peak for $0.2<|\mathbf{kl}|<0.5$, followed by broad, weak signals of decreasing intensity (lines are fits to a damped harmonic oscillator line shape with pole at finite energy). D: The width of the relaxational dynamics signal is linear in T, with a significant intercept at low temperature. The width of the dispersive peak at (1.5,1.5,-1.5) has an essentially identical temperature dependence. E: Summary of the nodal line dynamics, showing gapless behavior close to the pinch point, replaced by dispersive fast dynamics and weak broad scattering. The points and line indicate the dispersion of the susceptibility peak along both nodal lines and in both directions from the pinch point, folded into reduced units. The color map is an interpolation of the susceptibility measured in the constant wave vector scans (along $(h,h,-h)$). Error bars in B and C are derived from Poisson counting statistics of the measurement with scaling from $S(\mathbf{Q},\omega)$ to χ"$(\mathbf{Q},\omega)$. Error bars in D and E are the uncertainties of the least squares fitted parameters.

Materials and Methods [References 47-56]**:**

Our main sample is a single crystal of $CsNiCrF_6$, used and described in [25,26]. It is roughly cuboidal, with dimensions ≈6x8x12 mm. It was aligned by neutron Laue diffraction using Orient Express at the Institut Laue Langevin (ILL) (Grenoble, France) and mounted according to the intended experiment: glued to an aluminum finger with Quikfill (epoxy) for inelastic neutron scattering experiments at T>1.5 K; glued to a copper finger with Stycast (epoxy) for inelastic neutron scattering experiments at T< 1 K; wrapped in aluminum foil that was clamped to an aluminum finger for polarized diffuse neutron scattering experiments. Small pieces of dimension ≈0.5x1x2 mm that broke off the surface of the sample during ungluing were preserved and used for single crystal neutron diffraction experiments (glued to aluminum pins using Quikfill or GE varnish) or crushed for powder x-ray diffraction. We have a second crystal that has a well-developed octahedral form with edge dimension ≈5 mm. A small piece cut from this was also examined by x-ray powder diffraction.

For our synchrotron x-ray powder diffraction experiments, a piece of either crystal was mixed with silicon powder and ground together in an agate pestle and mortar. These mixtures were loaded into 0.3 mm glass capillaries. The silicon serves primarily to disperse small sample volume in the beam, and also provides a convenient calibrant for wavelength and lattice parameters (a_{Si}=5.431194 Å at 22.5°C, NIST powder diffraction standard 640c). We used the high-resolution powder diffractometer of the Materials Science Beamline [47] at the Swiss Light Source (SLS) (Paul Scherrer Institut, Villigen, Switzerland) to measure the diffraction pattern of the mixture. The diffractometer was operated in Debye-Scherrer geometry with Mythen microstrip detector and capillary spinner, the wavelength was 0.4959 Å (25 keV). The 2θ range extended from 7° to 120° without cryostat, or 7° to 80° with helium flow cryostat installed. We collected diffraction patterns at room temperature (24°C at the SLS) without the cryostat for the main sample, and between 5 K and 300 K with the cryostat for both. The powder diffraction data were normalized and reduced by standard routines, then modeled and fitted using the Rietveld method, as implemented in the package FullProf [47].

We carried out a single crystal neutron diffraction experiment using the quasi-Laue diffractometer VIVALDI [49] at the ILL. The sample was mounted in an `Orange' helium cryostat and cooled to T≈2.5 K. To ensure a full coverage of reciprocal space, the sample was rotated through 180° about the vertical axis, with 1-hour duration exposures recorded every 10°. The data were indexed and integrated using the program LAUEGEN [50], and wavelength normalized using LAUENORM [51]. The resulting integrated intensities were used for least squares refinement of crystallographic models using the package ShelXL [52]. A second single crystal neutron diffraction experiment was carried out using the monochromatic diffractometer TRiCS [53] at the Swiss Spallation Neutron Source (SINQ) (Paul Scherrer Institut, Villigen, Switzerland) in 4-circle mode. The sample was attached to the cold finger of a closed cycle cooling machine that was mounted on the Euler cradle. Using the germanium (Ge311) monochromator to provide neutrons of wavelength of 1.172 Å and a single ^{3}He tube detector, we measured 2550 reflections, with the temperature T=5 K throughout. Integrated intensities were combined and used for least squares refinement of crystallographic models using the packages Jana2000 and FullProf [54,47].

We measured and separated the magnetic and structural diffuse neutron scattering using the polarized neutron diffuse scattering spectrometer D7 [55] at the ILL. D7 was configured with wavelength λ=3.1 Å and Orange cryostat. The sample was mounted using aluminum foil to minimize incoherent scattering from glue, two strong Bragg peaks from the tails of the cryostat

contaminate the data and these areas are masked in the data analysis. We used the XYZ technique, which requires the measurement of non-spin flip and spin flip intensities for three orthogonal polarization directions, to separate the structural, spin incoherent, and magnetic cross sections. We rotated the crystal about the vertical axis in 0.5° steps, recording three complete rotations with the analyzer/detector banks offset in three non-overlapping positions and 17-18 s count time per channel, plus a further 270° rotation in one of the detector positions with 20 s count time. The sample was maintained at $T\approx1.8$ K throughout. We measured the background of the empty sample holder for each of the three detector positions with coarse rotation steps (18° or 30°) and 60 s counting times. The background was essentially angle independent so measurements at different rotation angles were combined and duplicated for subtraction from the sample data. Standard vanadium and quartz (silica glass) samples were used for normalization of detector and polarization analyzer efficiencies respectively. The nuclear, magnetic and spin incoherent cross sections were separated [55] and symmetrized by folding into a single quadrant of the scattering plane and then unfolding.

We report data from three inelastic neutron scattering experiments performed using the cold neutron triple axis spectrometer IN14 at the ILL. In the first, the sample was mounted in an Orange cryostat and cooled to $T\approx1.8$ K. The instrument was configured with PG002 monochromator and FlatCone analyzer. The FlatCone analyzer has 31 silicon (1,1,1) analyzer crystals, allowing to map the excitation spectrum at a single energy transfer. We recorded a 145° rotation of the sample (in 1° steps) with the analyzer bank offset at two positions. A measurement of the incoherent scattering from a vanadium sample was used to normalize the efficiency of the analyzer-detector channels. We performed two experiments in the conventional triple axis configuration with PG002 monochromator and analyzer. In one, the sample was cooled using the Orange cryostat, and our main collection of constant-wave vector scans at various reciprocal lattice positions and temperatures was made. In the other, the sample was cooled using a dilution refrigerator insert in the Orange cryostat to reach $T\approx0.07$ K, and a limited collection of scans was made. We estimate the energy resolution at the elastic line to be $\Delta E\approx0.1$ meV when $k_f=1.5$ Å^{-1} and $\Delta E\approx0.06$ meV when $k_f=1.3$ Å^{-1}.

Our numerical model of the structural diffuse scattering was encoded specifically by ourselves. The average crystal structure is built in a cubic supercell of the pyrochlore unit cell of size $L=6,12$. We establish an ice rule configuration of cations on the pyrochlore lattice by first tiling it with hexagonal loops (supercell sizes of $L=6,12$ are required to ensure complete coverage, such a tiling is illustrated in Ref. [56]). Starting in the lowest layer of the lattice, a hexagon-loop covering is constructed with probabilistic choice between two possible origins. On moving up to the next layer where sites are not covered by hexagons, the layer configuration is again chosen probabilistically. Once every site of the whole lattice is assigned to a hexagon, the covering can be permuted, again probabilistically, so that each possible growth direction of the hexagon coverage is equally represented. Within individual hexagons sites are assigned alternating up/down pseudo-spins, again choosing probabilistically between the two possible configurations. At this point, a specific ice-rule obeying pseudo-spin configuration has been generated, but one which does not have power-law correlations. The full power-law correlation function is obtained by propagating a large number of loop moves, allowing loops of any length and winding loops. Simulation of the magnetic neutron scattering pattern using spin configurations generated in this way will result in the $T=0$ scattering pattern of the pyrochlore Heisenberg antiferromagnet or spin ice, depending which type of spin is associated with the pseudo-spin configuration. For the structural simulation, pseudospin orientation is converted into cation identity, and we identify those tetrahedron edges with mixed cation pairs and shift

485 the relevant F^- anion towards its neighboring Cr^{3+} cation. Calculation of the bond valence sums
486 at this point reveals universal satisfaction of the requirements of Ni^{2+} and Cr^{3+}, but Cs^+ remains
487 unsatisfied. We search systematically around every cage center for positions that satisfy the
488 Cs^+ bond valence sum, within a certain tolerance, and with a certain resolution in spherical
489 polar coordinates, and tabulate all these positions. Then we choose positions for each Cs^+
490 randomly from its list and calculate the scattering pattern. The calculated data shown in Fig.
491 2B were obtained by repeating this procedure 200 times with L=12. The model intensities are
492 scaled and a constant background added to compare with the experimental data.
493
494 **Data availability:** The experimental data and their supplementary information, analyses and
495 computer codes that support the plots within this paper and the findings of this study are
496 available from the corresponding author upon reasonable request.
497
498 **Acknowledgments:** We thank Ross Stewart, Mark Green, and Bjorn Fåk for useful
499 discussions, John Chalker for reading and commenting on the manuscript, and Xavier Thonon
500 for support of cryogenics at the ILL. M. R. was supported by the SNSF (Schweizerischer
501 Nationalfonds zur Förderung der Wissenschaftlichen Forschung) (Grant No. 200021_140862).
502 This work is based on experiments performed at the Institut Laue Langevin, Grenoble, France;
503 the Swiss spallation neutron source SINQ, Paul Scherrer Institut, Villigen, Switzerland; and
504 the Swiss Light Source, Paul Scherrer Institut, Villigen, Switzerland.

505 **Author notes:** TF, MJH, SC, MB, PS, and STB carried our inelastic neutron scattering
506 experiments; TF, M.-HL-C, and OZ carried out neutron diffraction experiments; MR and AC
507 carried out x-ray diffraction experiments; TF analyzed all data and made calculations; TF,
508 MJH, and STB wrote paper in collaboration with all other authors.
509

510 **References and Notes:**

511 1. L. D. Landau, E. M. Lifshitz, Statistical Physics (Pergamon, New York, 1980).

512 2. D. Pekker, C. M. Varma, Amplitude/Higgs Modes in Condensed Matter Physics.
513 Annual Review of Condensed Matter Physics, **6**, 269–297 (2015).

514 3. C. L. Henley, The "Coulomb phase" in frustrated systems. Annual Review of
515 Condensed Matter Physics **1**, 179–210 (2010).

516 4. L. D. C. Jaubert, M. J. Harris, T. Fennell, R. G. Melko, S. T. Bramwell, P. C. W.
517 Holdsworth, Topological-Sector Fluctuations and Curie-Law Crossover in Spin Ice.
518 Physical Review X **3**, 011014 (2013).

519 5. D. Huse, W. Krauth, R. Moessner, S. L. Sondhi, Coulomb and liquid dimer models in
520 three dimensions. Physical Review Letters **91**, 167004 (2003).

521 6. M. Hermele, M. P. A. Fisher, L. Balents, Pyrochlore photons: The U(1) spin liquid in
522 a S=1/2 three-dimensional frustrated magnet, Physical Review B **69**, 064404 (2004).

523 7. O. Benton, O. Sikora, N. Shannon, Seeing the light: Experimental signatures of
524 emergent electromagnetism in a quantum spin ice. Physical Review B **86**, 075154 (2012).

525 8. M. J. P. Gingras, P. A. McClarty, Quantum spin ice: a search for gapless quantum spin
526 liquids in pyrochlore magnets. Reports on Progress in Physics **77**, 056501 (2014).

527 9. P. W. Anderson, Ordering and antiferromagnetism in ferrites. Physical Review **102**,
528 1008–1013 (1956).

10. P. A. McClarty, A. O'Brien, F. Pollmann, Coulombic charge ice. Physical Review B **89**, 195123 (2014).

11. R. Moessner, J. T. Chalker, Properties of a classical spin liquid: The Heisenberg pyrochlore antiferromagnet, Physical Review Letters **80**, 2929–2932 (1998).

12. S. V. Isakov, K. Gregor, R. Moessner, S. L. Sondhi, Dipolar spin correlations in classical pyrochlore magnets. Physical Review Letters **93**, 167204 (2004).

13. R. Moessner, J. T. Chalker, Low-temperature properties of classical geometrically frustrated antiferromagnets. Physical Review B **58**, 12049–12062 (1998).

14. P. H. Conlon, J. T. Chalker, Spin Dynamics in Pyrochlore Heisenberg Antiferromagnets. Physical Review Letters **102**, 237206 (2009).

15. P. H. Conlon, "Aspects of Frustrated Magnetism", thesis, Oxford University, Oxford (2010).

16. C. L. Henley, Power-law spin correlations in pyrochlore antiferromagnets. Physical Review B **71**, 014424 (2005).

17. T. Fennell, P. P. Deen, A. R. Wildes, K. Schmalzl, D. Prabhakaran, A. T. Boothroyd, R. J. Aldus, D. F. McMorrow, S. T. Bramwell, Magnetic Coulomb Phase in the Spin Ice $Ho_2Ti_2O_7$. Science **326**, 415–417 (2009).

18. M. J. Harris, S. T. Bramwell, D. F. McMorrow, T. Zeiske, K. W. Godfrey, Geometrical Frustration in the Ferromagnetic Pyrochlore $Ho_2Ti_2O_7$. Physical Review Letters **79**, 2554–2557 (1997).

19. C. Castelnovo, R. Moessner, S. L. Sondhi, Magnetic monopoles in spin ice. Nature **451**, 42–45 (2008).

20. I. A. Ryzhkin, Magnetic relaxation in rare-earth oxide pyrochlores. Journal of Experimental and Theoretical Physics **101**, 481–486 (2005).

21. A. R. Overy, A. B. Cairns, M. J. Cliffe, A. Simonov, M. G. Tucker, A. L. Goodwin, Design of crystal-like aperiodic solids with selective disorder–phonon coupling. Nature Communications **7**, 10445 (2016).

22. L. Shen, C. Greaves, R. Riyat, T. C. Hansen, and E. Blackburn, Absence of magnetic long-range order in Y_2CrSbO_7: Bond-disorder-induced magnetic frustration in a ferromagnetic pyrochlore, Physical Review B **96**, 094438 (2017).

23. Y. Li, D. Adroja, R. I. Bewley, D. Voneshen, A. A. Tsirlin, P. Gegenwart, and Q. Zhang, Crystalline Electric-Field Randomness in the Triangular Lattice Spin-Liquid $YbMgGaO_4$, Physical Review Letters **118**, 107202 (2017).

24. Z. Zhu, P. A. Maksimov, S. R. White, and A. L. Chernyshev, Disorder-Induced Mimicry of a Spin Liquid in YbMgGaO4, Physical Review Letters **119**, 157201 (2017).

25. M. J. Harris, M. P. Zinkin, T. Zeiske, Magnetic excitations in a highly frustrated pyrochlore antiferromagnet. Physical Review B **52**, R707–R710 (1995).

26. M. P. Zinkin, M. J. Harris, T. Zeiske, Short-range magnetic order in the frustrated pyrochlore antiferromagnet $CsNiCrF_6$. Physical Review B **56**, 11786–11790 (1997).

27. S. T. Banks, S. T. Bramwell, Magnetic frustration in the context of pseudo-dipolar ionic disorder. EPL (Europhysics Letters) **97**, 27005 (2012).

570 28. D. A. Keen, A. L. Goodwin, The crystallography of correlated disorder. Nature **521**,
571 303–309 (2015).

572 29. D. Babel, G. Pausewang, W. Viebahn, Die Struktur einiger Fluoride, Oxide und
573 Oxidfluoride AMe_2X_6 der $RbNiCrF_6$-Typ. Zeitschrift fuer Naturforshung, Teil B.
574 Anorganiche Chemie, Organishe Chemie **22**,1219-1220 (1967).

575 30. D. P. Shoemaker, R. Seshadri, A. L. Hector, A. Llobet, T. Proffen, C. J. Fennie, Atomic
576 displacements in the charge ice pyrochlore $Bi_2Ti_2O_6O'$ studied by neutron total scattering.
577 Physical Review B **81**, 144113 (2010).

578 31. See supplementary information.

579 32. T. R. Welberry, B. D. Butler, Interpretation of diffuse X-ray scattering via models of
580 disorder. Journal of Applied Crystallography **27**, 205–231 (1994).

581 33. R. B. Neder, T. Proffen, "Diffuse Scattering and Defect Structure Simulations: A cook
582 book using the program DISCUS" (Oxford University Press, Oxford, 2008).

583 34. J. A. M. Paddison, A. L. Goodwin, Empirical Magnetic Structure Solution of
584 Frustrated Spin Systems. Physical Review Letters **108,** 017204 (2012).

585 35. S. J. L. Billinge, I. Levin, The Problem with Determining Atomic Structure at the
586 Nanoscale. Science **316**, 561–565 (2007).

587 36. I. D. Brown, Recent Developments in the Methods and Applications of the Bond
588 Valence Model. Chemical Reviews **109**, 6858-6919 (2009).

589 37. V. V. Chernyshev, S. G. Zhukov, A. V. Yatsenko, L. A. Aslanov, and H. Schenk, The
590 use of Continuous Atomic Distributions in Structural Investigations. Acta
591 Crystallographica Section A: Foundations of Crystallography **50**, 601–605 (1994).

592 38. L. D. C. Jaubert, M. Haque, R. Moessner, Analysis of a Fully Packed Loop Model
593 Arising in a Magnetic Coulomb Phase, Physical Review Letters **107**, 177202 (2011).

594 39. M. O. Blunt, and J. C. Russell, M. D. C. Giménez-López, J. P. Garrahan, X. Lin, M.
595 Schröder, N. R. Champness, P. H. Beton, Random Tiling and Topological Defects in a
596 Two-Dimensional Molecular Network, Science **322**, 1077–1081 (2008).

597 40. J. L Jacobsen, F. Alet, Semiflexible Fully Packed Loop Model and Interacting
598 Rhombus Tilings, Physical Review Letters **102**, 145702 (2009).

599 41. L. Savary, L. Balents, Quantum spin liquids: a review. Reports on Progress in Physics
600 **80**, 016502 (2016).

601 42. K. W. Plumb, J. Hirtesh, J. Changlani, A. Scheie, Shu Zhang, J. W. Kriza, J. A.
602 Rodriuez-Rivera, Yiming Qui, B. Winn, R. J. Cava, C. L. Broholm, Continuum of quantum
603 fluctuations in a three-dimensional *S*=1 Heisenberg magnet.
604 https://arxiv.org/abs/1711.07509 (2017).

605 43. M. M. Koza, M. R. Johnson, R. Viennois, H. Mutka, L. Girard, D. Ravot, Breakdown
606 of phonon glass paradigm in La- and Ce-filled Fe_4Sb_{12} skutterudites. Nature Materials **7**,
607 805–810 (2008).

608 44. T. Shimojima, Y. Shibata, K. Ishizaka, T. Kiss, A. Chainani, T. Yokoya, T. Togashi,
609 X.-Y. Wang, C. T. Chen, S. Watanabe, J. Yamaura, S. Yonezawa, Y. Muraoka, Z. Hiroi,
610 T. Saitoh, S. Shin, Interplay of Superconductivity and Rattling Phenomena in β-Pyrochlore
611 KOs_2O_6 Studied by Photoemission Spectroscopy. Physical Review Letters **99**, 117003
612 (2007).

45. R. De Pape, G. Ferey, A new form of FeF_3 with the pyrochlore structure: Soft chemistry synthesis, crystal structure, thermal transitions and structural correlations with the other forms of FeF_3. Materials Research Bulletin **21**, 971–978 (1986).

46. S. W. Kim, S.-H. Kim, P. S. Halasyamani, M. A. Green, K. P. Bhatti, C. Leighton, H. Das, C. J. Fennie, $RbFe^{2+}Fe^{3+}F_6$: Synthesis, structure, and characterization of a new charge-ordered magnetically frustrated pyrochlore-related mixed-metal fluoride. Chemical Science **3**, 741–751 (2012).

47. P. R. Willmott, D. Meister, S. J. Leake, M. Lange, A. Bergamaschi, M. Böge, M. Calvi, C. Cancellieri, N. Casati, A. Cervellino, Q. Chen, C. David, U. Flechsig, F. Gozzo, B. Henrich, S. Jäggi-Spielmann, B. Jakob, I. Kalichava, P. Karvinen, J. Krempasky, A. Lüdeke, R. Lüscher, S. Maag, C. Quitmann, M. L. Reinle-Schmitt, T. Schmidt, B. Schmitt, A. Streun, I. Vartiainen, M. Vitins, X. Wang, R. Wullschleger. The Materials Science beamline upgrade at the Swiss Light Source. Journal of Synchrotron Radiation **20**, 667–682 (2013).

48. J. Rodriguez-Carvajal, Recent advances in magnetic structure determination. Physica B **192**, 55–69 (1993).

49. C. Wilkinson, J. A. Cowan, D. A. A. Myles, F. Cipriani, G. J. McIntyre, VIVALDI - A Thermal-Neutron Laue Diffractometer for Physics, Chemistry and Materials Science. Neutron News **13**, 37–41 (2002).

50. J. W. Campbell, Q. Hao, M. M. Harding, N. D. Nguti, C. Wilkinson, LAUEGEN version 6.0 and INTLDM. Journal of Applied Crystallography **31**, 496-502 (1998).

51. J. R. Helliwell, J. Habash, D. W. J. Cruickshank, M. M. Harding, T. J. Greenhough, J. W. Campbell, I. J. Clifton, M. Elder, P. A. Machin, M. Z. Papiz, S. Zurek, The recording and analysis of synchrotron X-radiation Laue diffraction photographs. Journal of Applied Crystallography **22**, 483–497 (1989).

52. G. M. Sheldrick. A short history of SHELX. Acta Crystallographica Section A: Foundations of Crystallography **64**, 112–122 (2008).

53. J. Schefer, M. Könnecke, A. Murasik, A. Czopnik, Th. Strässle, P. Keller, N. Schlumpf, Single-crystal diffraction instrument TriCS at SINQ. Physica B **276-278**, 168–169 (2000).

54. V. Petricek, M. Dusek, L. Palatinus, Crystallographic Computing System JANA2006: General features. Zeitschrift für Kristallographie 229, 345-352 (2014).

55. J. R. Stewart, P. P. Deen, K. H. Andersen, H. Schober, J.-F. Barthélémy, J. M. Hillier, A. P. Murani, T. Hayes, B. Lindenau. Disordered materials studied using neutron polarization analysis on the multi-detector spectrometer, D7. Journal of Applied Crystallography **42**, 69–84 (2008).

56. S.-H. Lee, C. Broholm, W. Ratcliff, G. Gasparovic, Q. Huang, T. H. Kim, S.-W. Cheong, Emergent excitations in a geometrically frustrated magnet. *Nature* **418**, 856–858 (2002).